Correspondence to:
K. Stergiopoulou,
katerina.strg@leicester.ac.uk

Solar Orbiter Data-Model Comparison in Venus' Induced Magnetotail

Katerina Stergiopoulou[1,2] [ID], **Riku Jarvinen[3,4]** [ID], **David J. Andrews[1]** [ID], **Niklas J. T. Edberg[1]** [ID], **Andrew P. Dimmock[1]** [ID], **Esa Kallio[3]** [ID], **Moa Persson[5]** [ID], and **Yuri V. Khotyaintsev[1]** [ID]

[1]Swedish Institute of Space Physics, Uppsala, Sweden, [2]School of Physics and Astronomy, University of Leicester, Leicester, UK, [3]School of Electrical Engineering, Aalto University, Aalto, Finland, [4]Finnish Meteorological Institute, Helsinki, Finland, [5]IRAP, CNRS-UPS-CNES, Toulouse, France

Abstract We investigate the structure of the Venusian magnetotail utilizing magnetic field and electron density measurements that cover a wide range of distances from the planet, from the first two Solar Orbiter Venus flybys. We examine the magnetic field components along the spacecraft trajectory up to 80 Venus radii down the tail. Even though the magnetic field behavior differs considerably between the two cases, we see extended electron density enhancements covering distances greater than $\sim$20 R_V in both flybys. We compare the magnetic field measurements with a global hybrid model of the induced magnetosphere and magnetotail of Venus, to examine to what degree the observations can be understood with the simulation. The model upstream conditions are stationary and the solution encloses a large volume of 83 $R_V \times$ 60 $R_V \times$ 60 R_V in which we look for spatial magnetic field and plasma variations. We rotate the simulation solution to describe different stationary upstream IMF clock angle cases with a 10° step and find the clock angle for which the agreement between observations and model is maximized along Solar Orbiter's trajectory in 1-min steps. We find that in both flybys there is better agreement with the observations when we rotate the model for some intervals, while there are parts that cannot be well reproduced by the model irrespective of how we vary the IMF clock angle, suggesting the presence of non-stationary features in the Venus-solar wind interaction not accounted for in the hybrid model.

1. Introduction

Early Venus missions, such as the Veneras and the Mariners, revealed the presence of a bow shock around Venus that encloses a smaller volume and is located much closer to the planet compared to Earth's bow shock, even though the two planets are of similar size, indicating the ionosphere of Venus as the effective obstacle to the solar wind (Russell et al., 1979a). Pioneer Venus Orbiter (PVO) probed the lower ionosphere and the solar wind-planetary interaction region (Luhmann & Cravens, 1991; Russell et al., 1979a). It was the first mission able to determine, by investigating the nightside of the planet and more specifically the planetary wake, the absence of an intrinsic magnetic field at Venus, through measurements of the magnetic field magnitude and direction which suggested a non-planetary origin of the magnetic field (Russell et al., 1979b). Even though the topology of the induced magnetotail is dictated by the orientation of the draped interplanetary magnetic field (IMF) (Russell et al., 1981), magnetic field variations were observed in the Venusian magnetotail that remained unexplained at the end of the PVO era (Phillips & McComas, 1991). Hemispherical plasma physical asymmetries were investigated intensively by using PVO observations (Luhmann, 1986; Russell et al., 2006) and thereafter with self-consistent kinetic computer simulations (Jarvinen et al., 2013; Kallio et al., 2006). The structure of the induced magnetotail and ion escape in the tail, and their dependence on the IMF orientation was investigated through PVO measurements by Slavin et al. (1989). More than a decade after the end of the PVO mission, Venus Express observations in the near-Venus magnetotail revealed the details of the plasma sheet formation and its dependence on the solar wind electric field (Dubinin et al., 2013), and IMF orientation and draping pattern (Masunaga et al., 2011). The hemispheric asymmetry caused by said dependence was further investigated by Rong et al. (2014), who additionally estimated the thickness of the current sheet. Furthermore, Zhang et al. (2009) have shown via a magnetohydrodynamic (MHD) simulation that if the IMF is aligned with the solar wind flow, then the whole induced magnetosphere disappears. Venus Express magnetic field measurements also enabled studies of the flapping motion in the Venusian magnetotail such as the work of Rong et al. (2015), where it was shown that the flapping can tilt the current sheet.

Since 2018, a series of Venus gravity assist maneuvers by NASA's Parker Solar Probe (PSP), ESA-JAXA's Bepi-Colombo and ESA's Solar Orbiter (SolO) missions have been providing new observations of the magnetotail at great distances from the planet. During PSP's fourth Venus flyby on 20 February 2021, the spacecraft crossed the wake region (Collinson et al., 2022). Collinson et al. (2022) present a revised structure of the induced magnetotail of Venus based on the observations of PSP compared with past studies with PVO, and results from a hybrid simulation. PVO first saw the filamentary nature of the nightside ionosphere at high altitudes comprised of comet-like tail rays, which may act as pathways for ion escape, however, it could not search for these structures at altitudes higher than 3,000 km (Brace et al., 1987; Collinson et al., 2022). The main tail rays signatures identified were electron density enhancements of cold ionospheric plasma, high plasma beta and rotations of the sunward component of the magnetic field (Brace et al., 1987; Collinson et al., 2022). These structures seen by PVO were also produced by a hybrid simulation by Brecht and Ledvina (2021). The simulation showed the formation, in the Venusian wake, of a single, broader tail ray the location of which is controlled by the IMF orientation in the ionosphere (Brecht & Ledvina, 2021; Collinson et al., 2022). Collinson et al. (2022) proposed the formation of a single tail ray as a transient phenomenon in the induced magnetotail and they showed that such a structure can reach altitudes of 7,800 km, greater than one Venus radius, R_V, where $R_V = 6,052$ km is the radius of Venus used in this work. BepiColombo during its first Venus flyby on 15 October 2020, traveled along the magnetotail, down to 48 R_V (~300,000 km), in contrast to PSP trajectory that only crossed it (Mangano et al., 2021; Volwerk, Sánchez-Cano et al., 2021). Due to a coronal mass ejection (CME) preceding BepiColombo's first flyby, a particularly active magnetotail was recorded with a flapping motion of a ~7 min period (Volwerk, Sánchez-Cano et al., 2021).

The SolO mission plans include a total of seven Venus flybys from which the first two occurred on 27 December 2020 and on 9 August 2021 (Müller et al., 2020). Rare measurements deep in the induced magnetotail, down to at least 80 R_V, provide us with the opportunity to look at the structure of the far magnetotail, a region only probed before by Mariner 10, Galileo and BepiColombo (Kivelson et al., 1991; Lepping & Behannon, 1978; Volwerk, Sánchez-Cano et al., 2021). In these first two flybys, SolO travels through the magnetotail for several hours unlike PSP which was located in the wake for approximately 10 min (Collinson et al., 2022; Müller et al., 2020). During the first flyby the Radio and Plasma Waves (RPW) instrument (Maksimovic et al., 2020) detected electromagnetic whistler waves, electrostatic electron phase-space holes, ion acoustic waves and Langmuir waves for the first time continuously from the bow shock to the far tail region (Hadid et al., 2021). Suprathermal energetic ions were measured throughout the first flyby and various particle acceleration processes were observed (Allen et al., 2021), while the structure of the bow shock was studied in detail by Dimmock et al. (2022). Additionally, magnetic field observations were carefully analyzed by Volwerk, Horbury, et al. (2021), revealing various structures such as flux ropes and magnetic reconnection sites.

The SolO flybys in the distant tail could possibly reveal the location of a boundary region where the induced magnetotail ends and the undisturbed solar wind dominates again. What's more, utilizing magnetic field data, we will be able to spot the locations, if any, where boundary crossings occurred throughout the flybys, due to either expansion or shrinking of the interaction region, while density observations could point to density blobs indicating plasma escape. The first two Venus flybys investigated in this study are unique in that SolO travels along the magnetotail to great distances, whereas in future scheduled SolO Venus flybys as well as in PSP and BepiColombo Venus flybys the spacecraft either does not reach that far in the magnetotail or only travels across the tail.

The far Venus magnetotail remains mostly unexplored due to the lack of measurements. Limited modeling work has been done there because of the computational expense of the large simulation domains, and even so, there has not been much data with which to compare it. In this paper, we take advantage of the new SolO flyby data to shed light on this region. We examine electron density and magnetic field measurements from the first (Venus Gravity Assist Maneuver—VGAM1) and second (VGAM2) SolO Venus flybys and compare the observations with a hybrid simulation. In Section 2, we present SolO's observations in the induced magnetotail of Venus, in Section 3 we describe the hybrid simulation, the results of which we utilize to obtain a clearer picture of the tail through the comparison with the data and to see how well the data can be interpreted with the model in this region, and in Section 4 we explain the process we follow to compare the measurements with the model. The results of the comparison between the observations and the model are shown in Section 5, while in Sections 6 and 7 a discussion of the results and the final conclusions of the study follow, respectively.

2. Observations

We use SolO electron density data and magnetic field measurements from VGAM1 on 27 December 2020 and VGAM2 on 9 August 2021. The fluxgate magnetometer (MAG) on board SolO, which consists of two sensors mounted on the spacecraft boom, is dedicated to measuring the IMF vector with a nominal resolution of 4 pT while in the range of ±128 nT, and it can produce up to 128 samples/sec depending on the mode it operates (Horbury et al., 2020). In this study we use "normal" mode measurements of 8 samples/sec. The electron density data utilized throughout this paper are derived from the probe-to-spacecraft potential measured by the RPW instrument (Maksimovic et al., 2020) as described by Khotyaintsev et al. (2021).

In Figure 1, we show the trajectories of the flybys in the planet centered Venus Solar Orbital (VSO) coordinate system, where the $X_{\rm VSO}$ axis points toward the Sun, the $Z_{\rm VSO}$ axis is oriented parallel to the normal vector of Venus' orbital plane and the $Y_{\rm VSO}$ axis completes the right-handed system pointing approximately antiparallel to the orbital velocity of Venus. VGAM1 and VGAM2 are presented in blue and red, respectively in (a) cylindrical VSO coordinates, in the (b) XY VSO plane and in the (c) XZ VSO plane. The solid and dotted lines represent the bow shock and the upper mantle boundary (UMB), respectively, based on the model by Martinecz et al. (2009). We also mark with X symbols the time on the trajectories for both flybys every 80 min as in Figure 1 by Hadid et al. (2021), and with star symbols two features and three rotations in the first and second flyby, respectively, the details of which will be explained in the next paragraphs. SolO crosses the bow shock during VGAM1 in 2020-12-27 at ~12:40 UTC and during VGAM2 in 2021-08-09 at ~04:41 UTC. Looking at Figures 1a and 1b we notice that the trajectories of the two flybys are outwardly similar to each other. However, Figure 1c reveals a significant divergence between the two flybys in the $Z_{\rm VSO}$ direction. In both cases SolO flew along the Venusian magnetotail before eventually leaving the system after it has passed through the bow shock. SolO remained marginally closer to the central axis of the tail ($Y_{\rm VSO} = Z_{\rm VSO} = 0$) during VGAM1 compared to VGAM2 in the inbound segment of the flyby, to distances of ~22 R_V down the tail. Here, we only analyze data coming no farther than $X_{\rm VSO} = -80\,R_V$.

An overview of the VGAM1 measurements is illustrated in Figure 2. We present time series of the electron density, n_e, in Figure 2a, and of the magnetic field components, B_X, B_Y, B_Z, and magnitude, $|B|$, in Figures 2b–2d and 2e, respectively, as the spacecraft travels toward Venus. The dashed vertical line represents the bow shock crossing at ~12:40 UTC. Below the time axis, we also indicate the $X_{\rm VSO}$ coordinate in R_V. The 8 Hz MAG data has been re-sampled, thus the data displayed in all panels is of 1 Hz cadence. Beyond ~$-60\,R_V$ the magnetic field appears rather steady, resembling the upstream solar wind in both magnitude and orientation, while closer to the planet, fluctuations in the magnetic field with amplitudes of a few nT are present up to the bow shock, consistent with passage through the downstream Venusian magnetosheath. These fluctuations are interrupted at least on two occasions by short undisturbed intervals, most easily noticed in the B_X component, at approximately few minutes before ~06:00 UTC and a few minutes after ~08:00 UTC indicated in Figure 2b by **I** and **II**, respectively. The beginning of the former interval coincides with a jump in electron density. A substantial deviation in both magnitude and orientation of the field associated with the near-field of Venus-solar wind interaction is seen at closest approach, and has been studied in more detail, for example, by Volwerk, Horbury, et al. (2021).

In Figure 3, VGAM2 measurements are presented following the same format as previously in Figure 2. The structure of the magnetic field is steadier than in VGAM1, and there is not a clear point beyond which the magnetic field behavior changes, particularly with respect to the higher-frequency components of the field. Thus, we cannot make any assumptions about the distance where the solar wind starts to dominate, and transition from the unperturbed solar wind far downstream from Venus to the shocked solar wind of the magnetosheath is not identifiable. Three distinct rotations can however be seen in the field data shown in Figure 3b in the B_X component (a rotation can be identified as a change in vector components with the total field magnitude staying ~constant), at approximately ~20:00 UTC, a few minutes before ~00:00 UTC and a few minutes before ~03:00 UTC, denoted in Figure 3b by **I**, **II** and **III**, respectively. The interval between the two latter rotations coincides with an increase in the electron density, and a dip in electron density occurs during the second rotation as shown in Figure 3a. Having only single-point measurements available for both these flybys and no real-time knowledge of the upstream conditions, we instead turn to a detailed comparison with the outputs of a simulation of the Venus-solar wind interaction to further analyze and interpret these observations as well as test the validity of the model.
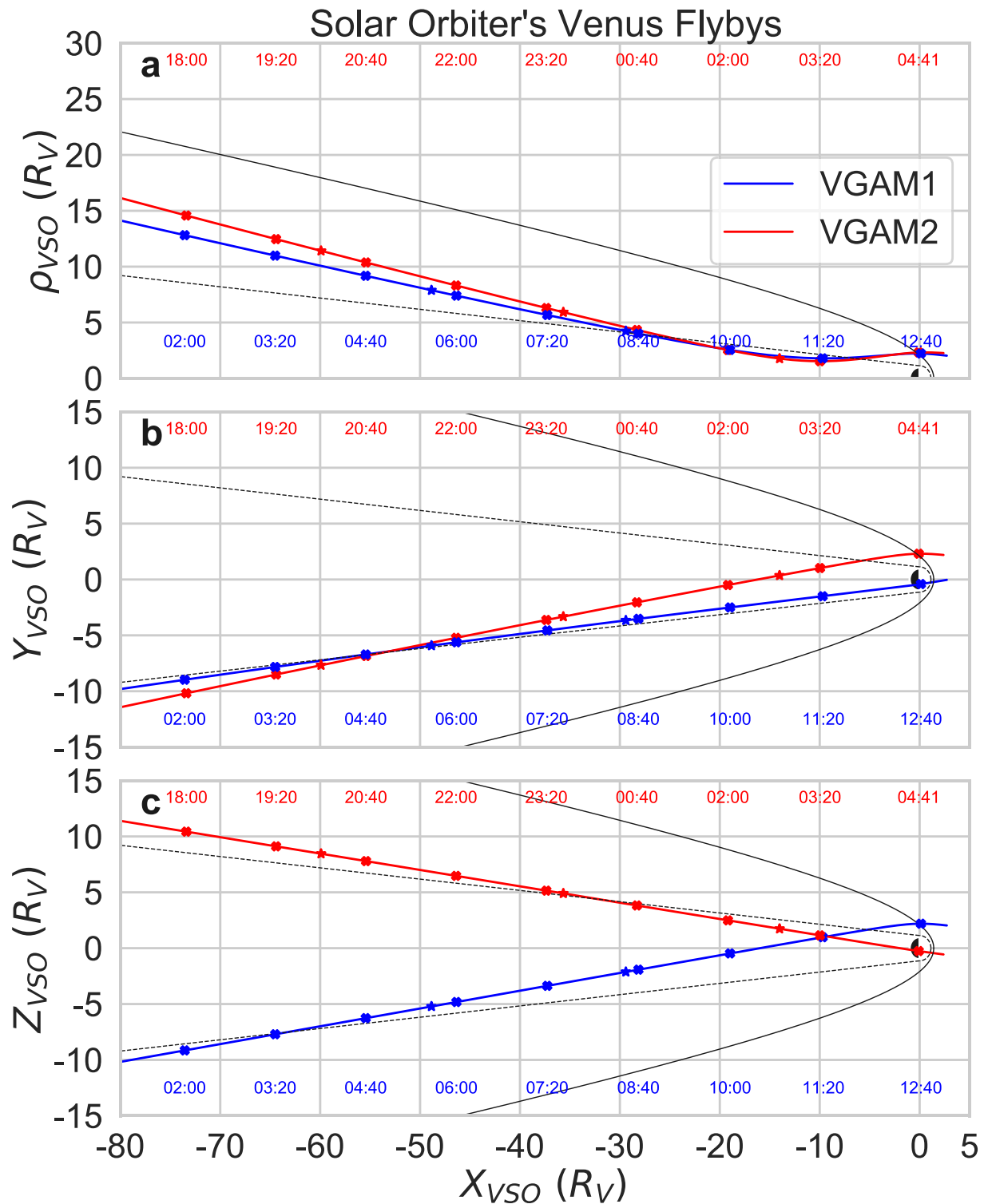
Figure 1. The first (VGAM1, 27 December 2020) and second (VGAM2, 9 August 2021) SolO Venus flyby trajectories in blue and red, respectively, in VSO (a) cylindrical coordinates where $\rho = \sqrt{Y^2 + Z^2}$, (b) projected on the XY plane and (c) projected on the XZ plane. The solid and dotted lines depict the bow shock and the upper mantle boundary (UMB) based on the model by Martinecz et al. (2009).
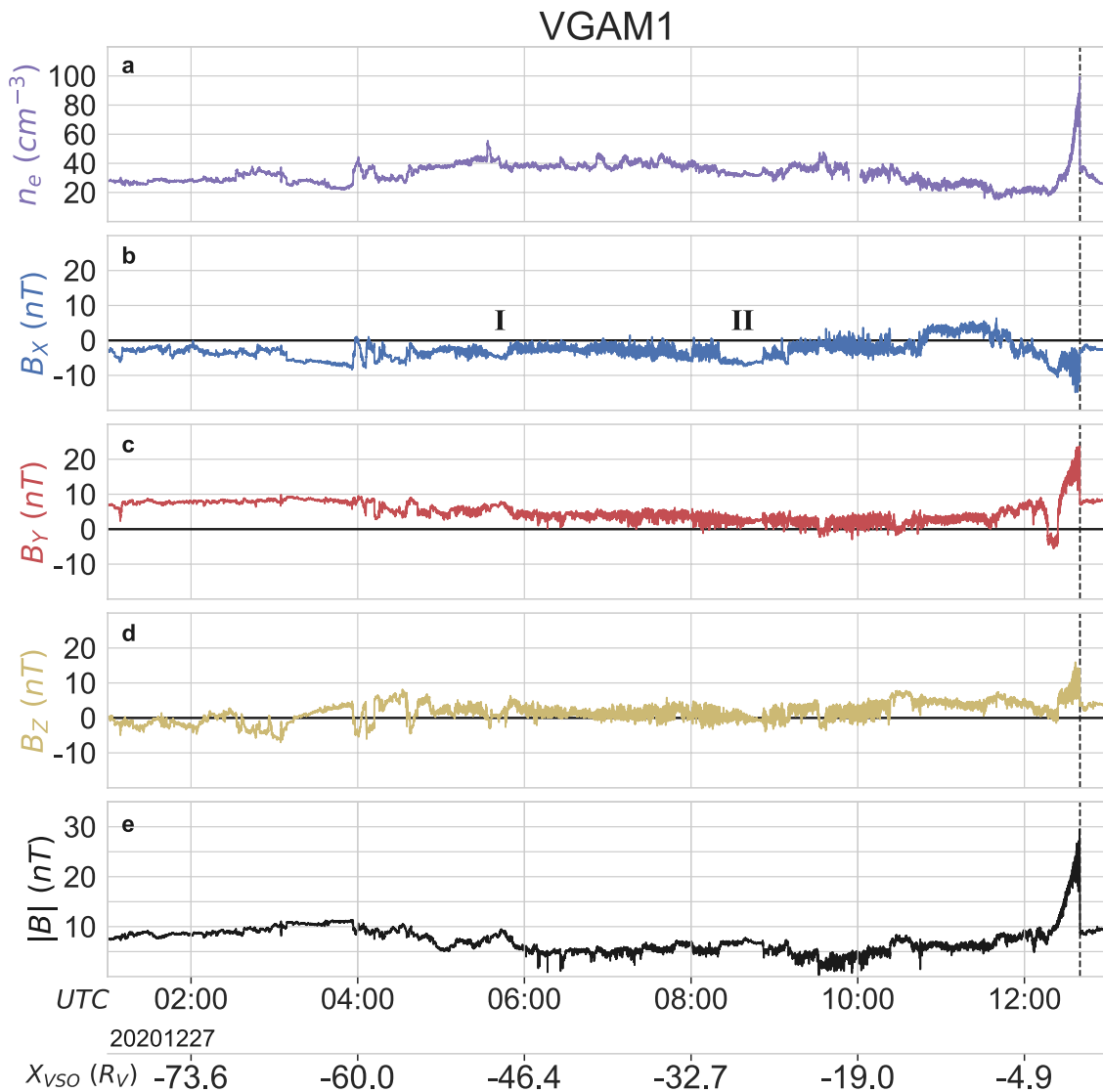
Figure 2. Time series of (a) electron density, (b)-(d) magnetic field components and (e) magnitude from the first SolO Venus flyby (VGAM1). The dashed vertical line shows the time of the bow shock crossing by the spacecraft at ~12:40 UTC. An axis showing the X_{VSO} component along the trajectory has been added below the time one.

3. Model

In addition to the SolO observations, the results of the global hybrid simulation RHybrid, described in Jarvinen et al. (2018), are utilized as a means to further investigating the structure of the magnetotail of Venus and the Venus-solar wind interaction through the comparison with the real data. The model setup is similar to earlier studies (Jarvinen et al., 2020, 2022) except here we use a larger simulation domain than before to allow the analysis of the far Venus tail. The Lorentz force determines the motion of solar wind and planetary ions, which are treated as macroscopic particle clouds (macroparticles), while electrons are modeled as a charge-neutralizing and massless adiabatic fluid (Jarvinen et al., 2020). Ion dynamics are self-consistently coupled with the evolution of the magnetic field via ion electric charge density and ion electric current density in the electric field in Faraday's law. This means that, for example, the solar wind mass-loading by planetary plasma is included in the model self-consistently. The solar wind ion species consist of protons and 4% of alpha particles. Exospheric photoions are created from the hydrogen and oxygen neutral corona, and ionospheric oxygen ions are emitted from model's inner boundary (Jarvinen et al., 2018, 2020). The solar wind and IMF conditions are assumed to be stationary and the upstream IMF vector is determined by SolO measurements, specifically the 10 minute average value in the upstream solar wind after the spacecraft crossed the outbound bow shock. The model was run until the solution
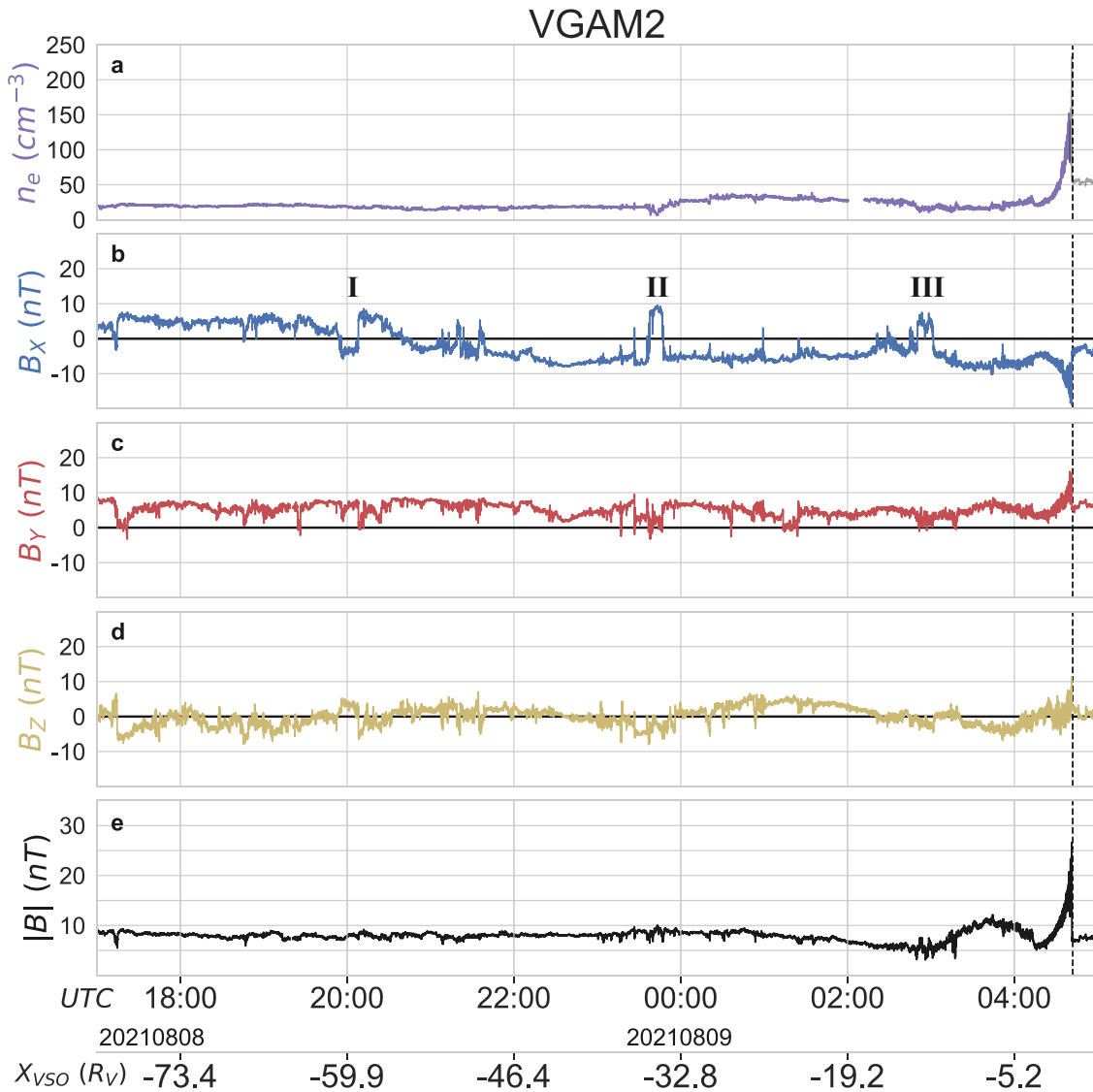
Figure 3. Time series of (a) electron density, (b)-(d) magnetic field components and (e) magnitude from the second SolO Venus flyby (VGAM2). The dashed vertical line shows the time of the bow shock crossing by the spacecraft at ~04:41 UTC. An axis showing the X_{VSO} component along the trajectory has been added below the time one.

reached a quasi-stationary state of development where there were no evident changes occurring. The analyzed simulation variables were averaged over 50 s in internal simulation time to smooth noise associated with statistical macroparticle fluctuations. The upstream magnetic field and solar wind conditions (Dimmock et al., 2022) and details of the simulation run setup are given in Table 1. In Figure 4, we show the overview of the simulation results including the solar wind proton density, n (Figures 4a–4c), magnetic field magnitude, $|B|$ (Figures 4d–4f), and the X component of the magnetic field, B_X (Figures 4g–4i). Note that the coordinates are in the VSO system. The ~6° aberration caused by Venus' orbital motion is neglected. The unit of length is the radius of Venus (R_V).

In this large simulation domain, the bow shock is readily identified in all panels as an increase in plasma density and magnetic field strength. Moreover, it appears modestly asymmetric with respect to the solar wind density in the XY plane (Figure 4a) owing to the non-zero B_X component present in the IMF. The rarefaction in the immediate wake of Venus is also clearly present out to the boundary of the simulation domain. The so-called magnetic "lobe" structure in the X-component of the magnetic field can also be identified, generated as part of the draping of IMF field lines around and through the Venusian ionosphere, forming a bi-polar signature in B_X in the induced magnetotail. Again, this feature is modestly asymmetric owing to the non-zero B_X component of the IMF, leading

Table 1
Global Hybrid Model Setup, Undisturbed Upstream Solar Wind (SW) and Interplanetary Magnetic Field (IMF) Conditions

Parameter	Value
Box size ($X \times Y \times Z$) [R_V]	$(-80...3) \times (-30...30) \times (-30...30)$
Number of grid cells ($n_X \times n_Y \times n_Z$)	$332 \times 240 \times 240$
Grid cell size	$(1512.95\,\text{km})^3 = (R_V/4)^3$
Number of macroparticles	106 per cell on average
Timestep	0.1 s
SW bulk velocity vector [v_X, v_Y, v_Z]	$[-325,0,0]$ km/s
H_{sw}^+ temperature	10^5 K
He_{sw}^{++} temperature	3.5×10^5 K
H_{sw}^+ density	20 cm^{-3}
He_{sw}^{++} density	0.8 cm^{-3}
Electron temperature	10^4 K
IMF vector [B_X, B_Y, B_Z]	$[-2.1,7.9,3.4]$ nT
IMF magnitude $|B|$	8.85 nT
Superconducting shell radius (R_η)	6351.8 km $= R_V + 300$ km
Obstacle resistivity ($r < R_\eta$)	0
Plasma resistivity ($r \geq R_\eta$)	$4.2 \times 10^{-3} \times \mu_0 \Delta x^2 / \Delta t$
Particle absorption radius	6251.8 km $= R_V + 200$ km
H_{exo}^+ photoion prod. rate	6.42×10^{24} s^{-1}
O_{exo}^+ photoion prod. rate	4.09×10^{24} s^{-1}
O_{iono}^+ ionospheric emis. rate	1.0×10^{25} s^{-1}
Ionospheric emis. radius	$R_V + 400$ km
Solar EUV photon rates	solar minimum

to a relatively smaller volume of positive (sunward) fields in the tail than negative (anti-sunward) fields. This asymmetry is particularly evident in the rightmost panels, showing a planar cut through the tail at $X = -10R_V$.

To better visualize the draping of the IMF around Venus and the extent of the influence of the planetary obstacle on the solar wind, we illustrate, in Figure 5, the IMF lines around Venus, extracted from the simulation domain shown in Figure 4. Specifically, in Figures 5a and 5b we show field lines draping around the planet from the dayside near the planet, where the strongest draping occurs, to far down the tail, where the field lines curvature releases. In Figure 5a these are shown from a 3-D view angle from the dayside toward the planet, along with color-coded magnetic field strength in the XY and XZ planes, while in Figure 5b the same field lines are shown in a view angle straight toward the plane containing the undisturbed IMF and solar wind velocity vectors. In Figures 5c and 5d, the field line tracing starts along the SolO VGAM1 trajectory, noting that this plane is not perfectly flat. Thus, these panels give the magnetic field connection to the spacecraft within the simulation domain. As is seen upstream, these field lines are regular and straight in the IMF, prior to their interaction with the Venus system, while they become draped, piled up and distorted as they interact with the ionosphere, before eventually largely 'straightening out' again some 10s of R_V down-tail. However, perturbations in these field lines are still evident in these simulation results out to the bow shock, throughout the simulation domain. Figures 5e and 5f show 100 field lines the tracing of which started on the spherical surface with radius $r = R_V + 500$ km. These field lines are connected near the inner boundary of the model and imply a magnetic connection to the ionosphere. The field draping around the obstacle shows a typical structure of the Venusian induced magnetosphere (Jarvinen et al., 2013; McComas et al., 1986; Saunders & Russell, 1986; Terada et al., 2009). Figures 5e and 5f show that the SolO VGAM1 trajectory does not cross field lines connected near the model's inner boundary and the ionosphere. Furthermore, these field lines do not extend far in the deep tail.

4. Comparison Between Observations and Model

The simulation of the Venus solar wind interaction presented in Section 3 is now used as a "reference" against which the observations made by SolO can be quantitatively examined. Differences between the model-predicted and observed magnetic field in the Venus tail can be caused by many factors, most notably time-variations in the upstream conditions (IMF strength and direction, and bulk solar wind parameters such as density and velocity). However, Venus' lack of any internal magnetic field, rapid response to solar wind variations and axially symmetric inner boundary and planetary upper atmospheric conditions (dependence only on the solar zenith angle) in the analyzed hybrid model run make it justifiable to "approximate" different stationary IMF clock angle (the orientation of the IMF component perpendicular to the upstream solar wind velocity) cases by simply rotating the simulation solution about the X-axis by an appropriate angle α, avoiding the need to completely re-run the simulation to examine the results of such rotations. Applying such a rotation can equally well be interpreted as rotating the entire trajectory of SolO about the X-axis by an angle $-\alpha$ and transforming the vector fields accordingly with an opposite rotation. Note that rotating the simulation solution can only describe changes in the IMF clock angle in a stationary sense and no possible dynamical interactions associated with them are included. Moreover, changes in the upstream IMF B_X component, the Parker spiral angle or the IMF magnitude cannot be estimated like this.

In order to compare the model magnetic field data with the SolO observations, we extract the simulation results at the location of SolO throughout the flybys. Specifically, we extract bulk parameters by interpolating the simulation results along the SolO trajectories, after rotating the simulation domain about the X-axis through angles α in 10° steps from 0° to 350°. We calculate the mean values of the measured magnetic field components for each minute along the trajectories and compare them with the same spatial averages of the model data. The upstream
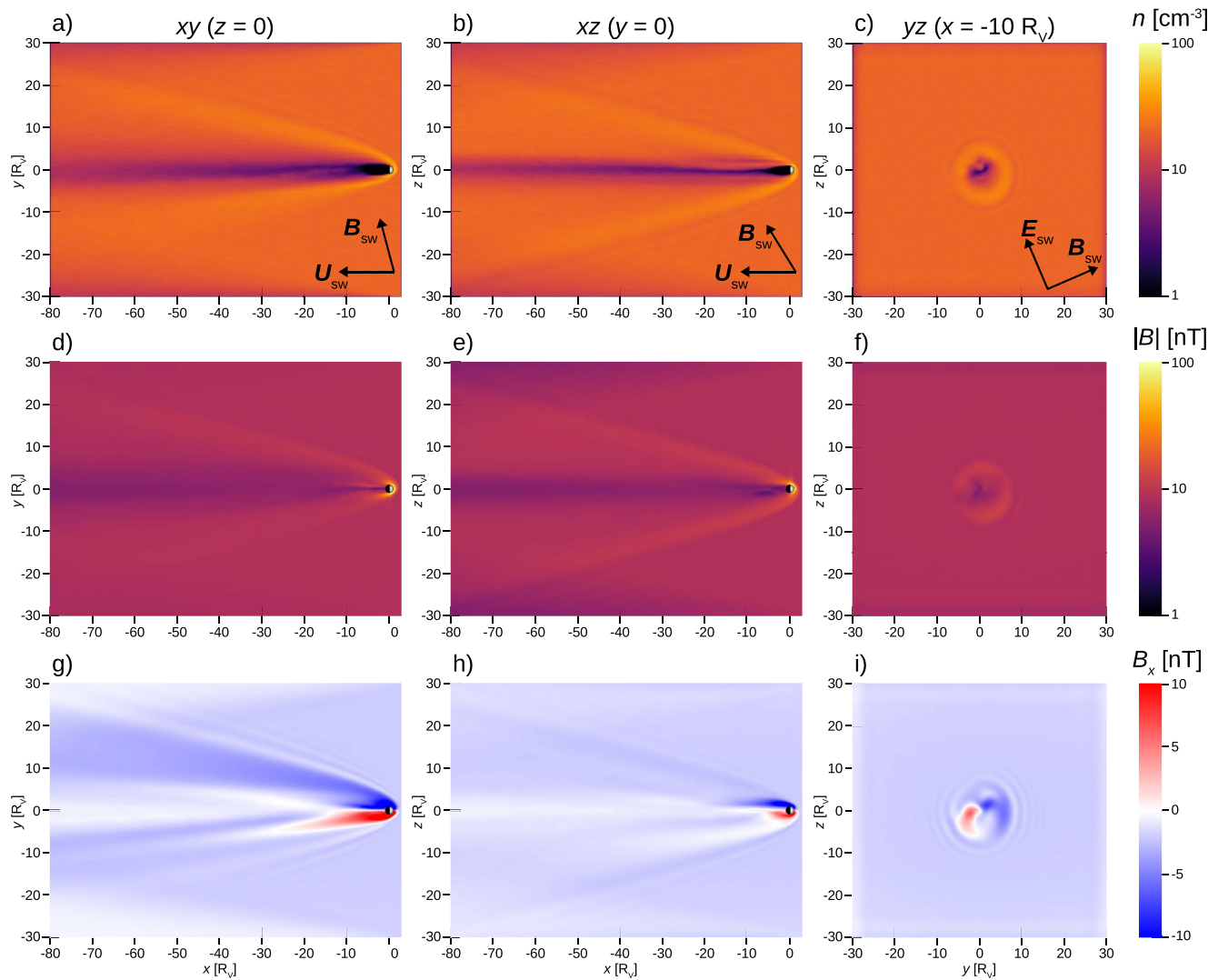
Figure 4. Simulation results of the solar wind-Venus interaction. Solar wind density in XY, XZ and YZ VSO planes in (a)–(c), magnetic field magnitude in (d)–(f) and the X component of the magnetic field, B_X, in (g)–(i).

conditions are not substantially different during the two flybys (VGAM2, $\mathbf{B}$ = [−3.0, 6.6, 0.6] nT), thus we use simulation data from the same run (Table 1) to compare with both VGAM1 and VGAM2.

Having generated model data for different IMF clock angles (simulation solution rotated with an angle α around the X-axis) with respect to the upstream IMF orientation that range from 0° to 350° with a 10° step, besides comparing the observations to the default simulation data, which corresponds to rotation angle zero ($\alpha = 0$), we also look for the optimal rotation angle, α_{opt}, at each point along the trajectory. While various alternative schemes can be used, we here chose to define α_{opt} as the model rotation angle for which the angle θ between the rotated model magnetic field vector ($\mathbf{B}_{opt}$) and the measured magnetic field vector ($\mathbf{B}_{obs}$) is minimum, $\theta_{min} = \arccos\left(\frac{\mathbf{B}_{opt} \cdot \mathbf{B}_{obs}}{|\mathbf{B}_{opt}||\mathbf{B}_{obs}|}\right)$. Ideally, θ_{min} should be equal to 0° but this is not always achieved. A similar analysis and comparison between Venus data and a hybrid simulation can be found in the work of Dimmock et al. (2018).

In Figure 6, we show, for simplicity, the projection of the magnetic field vectors to the YZ VSO plane, and the aforementioned angles between the model and the observations, valid at any moment within the flyby. $\mathbf{B}_{obs}$ is the vector of the magnetic field measured by SolO, $\mathbf{B}_{model}$ is the default magnetic field vector from the simulation run in the stationary state without any additional rotation of its components ($\alpha = 0$) and $\mathbf{B}_{opt}$ is the model magnetic field vector which best agrees with the observed magnetic field, that is, the vector that forms the smallest angle,
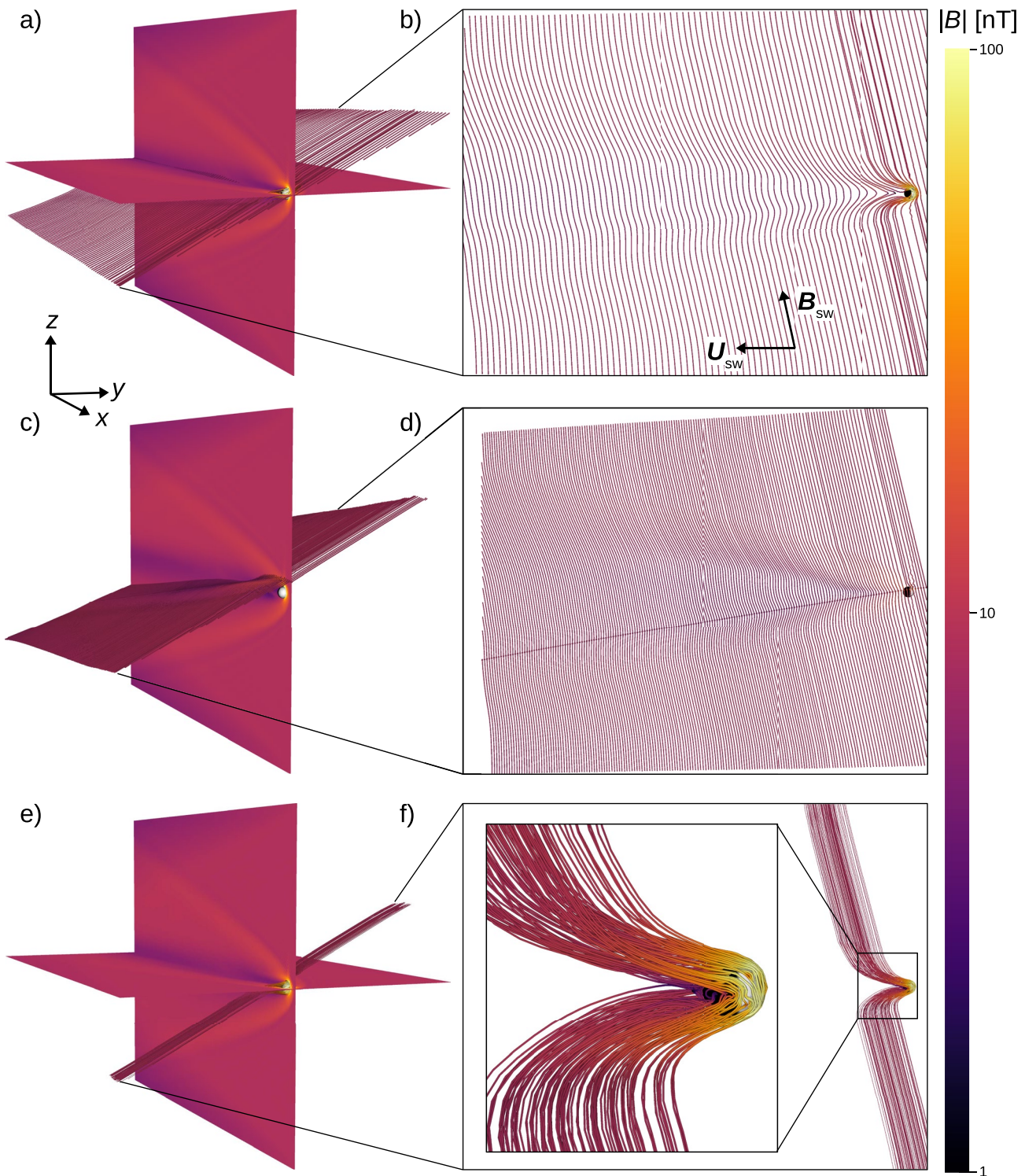
Figure 5. Illustration of 3-D IMF field lines in the Venusian induced magnetosphere in the global hybrid simulation. (a) and (b) give an overview of the field lines' morphology, while (c) and (d) show the field lines' tracing beginning along SolO's VGAM1 trajectory, which is depicted as black dots. Panels (e) and (f) show the field lines connected on the $R = R_V + 500$ km sphere. The magnetic field strength is represented color-coded on field lines and surfaces (panels a and e: $y = 0$ and $z = 0$ planes, panel c: $y = 0$ plane).
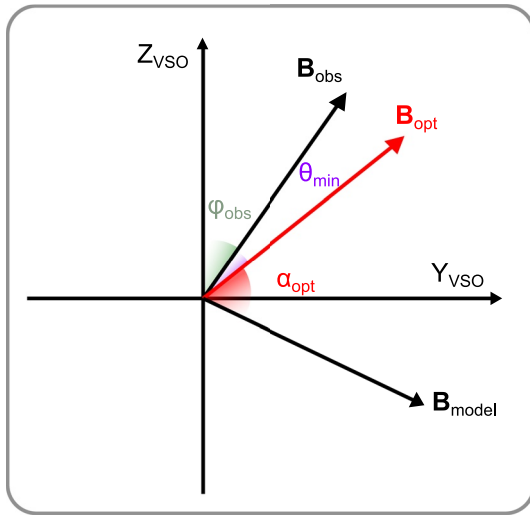
Figure 6. Measured $\mathbf{B}_{obs}$, default model $\mathbf{B}_{model}$ and optimum model $\mathbf{B}_{opt}$ magnetic field vectors projected in the YZ VSO plane for a random moment along the spacecraft trajectory. Note that we analyze a stationary simulation solution and thus, $\mathbf{B}_{model}$ and $\mathbf{B}_{opt}$ are time independent. The angles φ_{obs}, θ_{min}, and α_{opt} are the measured clock angle, the minimum possible angle between observations and model and the additional rotation of the model about the default model vector, respectively.

θ_{min}, with the observed magnetic field. The angles φ_{obs}, θ_{min}, and α_{opt} depicted in the Figure are the clock angle of the measured magnetic field, the minimum possible angle between the observed and the model magnetic field, and the optimum rotation of the model magnetic field with respect to the default one, respectively.

To further clarify the derivation of α_{opt}, we present, in Figure 7, example calculations performed at a specific moment of VGAM1 (2020-12-27, 11:03:00 UTC). We plot the modeled magnetic field components, B_X, B_Y, and B_Z as blue, red, and yellow dots, respectively, versus the rotation α applied to the simulation. On the same plot we superimpose the magnetic field measured by SolO, B_{X_obs}, B_{Y_obs}, and B_{Z_obs} as blue, red and yellow horizontal lines, respectively. For each rotation α, corresponding to a rotation of the location of SolO, a new magnetic field value is extracted from the simulation, and the angle θ between the magnetic field vector from SolO (solid lines in Figure 7) and the model magnetic field vector is calculated. The minimum value of θ, (θ_{min}), thus defines the best possible agreement between the model and the observed field that can be obtained by this rotation process, found after a rotation we label α_{opt}. The dashed vertical gray line in Figure 7, indicates α_{opt}, which is 30° in this example. The angle θ_{min} that we use to evaluate the agreement between observations and data in this example is $\theta_{min} = 48°$ (not shown in the figure).

5. Results

5.1. VGAM1

Having derived α_{opt}, θ_{min}, and $\mathbf{B}_{opt}$ as described above, we then proceed to compare the magnetic field components SolO measures during VGAM1 with both the "default" model output $\mathbf{B}_{model}$, having had no rotation applied (i.e., $\alpha = 0$ at all times), and the optimized model results $\mathbf{B}_{opt}$, as composed only by the values evaluated after the optimum rotation α_{opt} is applied for each one-minute interval along the flyby trajectory. We show in Figures 8a and 8b, the electron density (with 1 Hz cadence) and the one-minute averages of the magnetic field components and magnitude from SolO, respec-

tively. The solar wind density from the model as well as the density based on the optimized magnetic field vectors are superimposed in Figure 8a. In Figure 8c, α_{opt} is plotted with θ_{min} shown color-coded for each point along the spacecraft's trajectory. Thus, intervals for which a good agreement with the model was obtained after a rotation was applied are shown with blue colors (low values of θ_{min}), while intervals where only a poor agreement could be obtained even after optimizing the rotation angle are shown with red colors (high values of θ_{min}). We note that, as follows from the definitions above together with the selection of the upstream parameters for the underlying simulation run, both $\theta_{min} \approx 0°$ and $\alpha_{opt} \approx 0°$ in the solar wind upstream, indicating (unsurprisingly) that a good agreement between the modeled and observed fields exists here.

In Figures 8d–8f, we show in blue, red and yellow the measured magnetic field components, and in each panel the optimum magnetic field component and the model magnetic field component for zero rotation angle ($\alpha = 0$) are over-plotted as thin and thick gray lines, respectively. Additionally to the UTC time of the flyby as the X axis, a secondary axis demarcating the X_{VSO} component of SolO's trajectory is displayed. Based on the observations and the θ_{min} angle we note with five black lines labeled t_{a1}-t_{a5}, the points where both the behavior of the magnetic field and the degree to which there is agreement between the model and the observations change, indicating possible transitions between different regions in the interaction, or transient variations
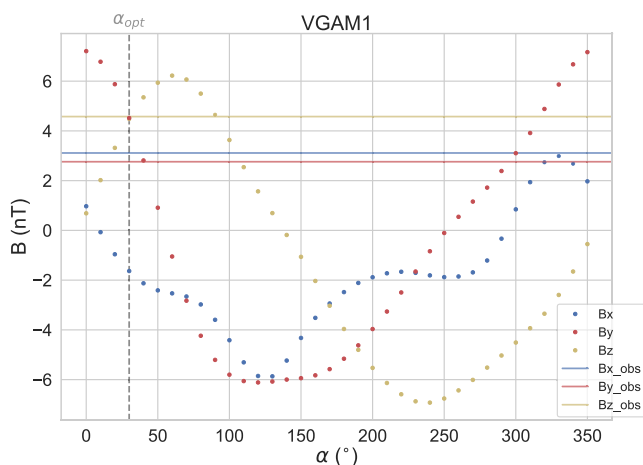

Figure 7. Example of a magnetic field snapshot of a selected moment (2020-12-27, 11:03:00 UTC) during VGAM1. The modeled magnetic field components versus the rotation, α, applied to the simulation are depicted as blue (B_X), red (B_Y), and yellow (B_Z) dots. The blue (B_{X_obs}), red (B_{Y_obs}), and yellow (B_{Z_obs}) solid lines show the observed magnetic field components for the specific moment. The dashed vertical gray line represents α_{opt} derived from the magnetic field vectors as described in the text.
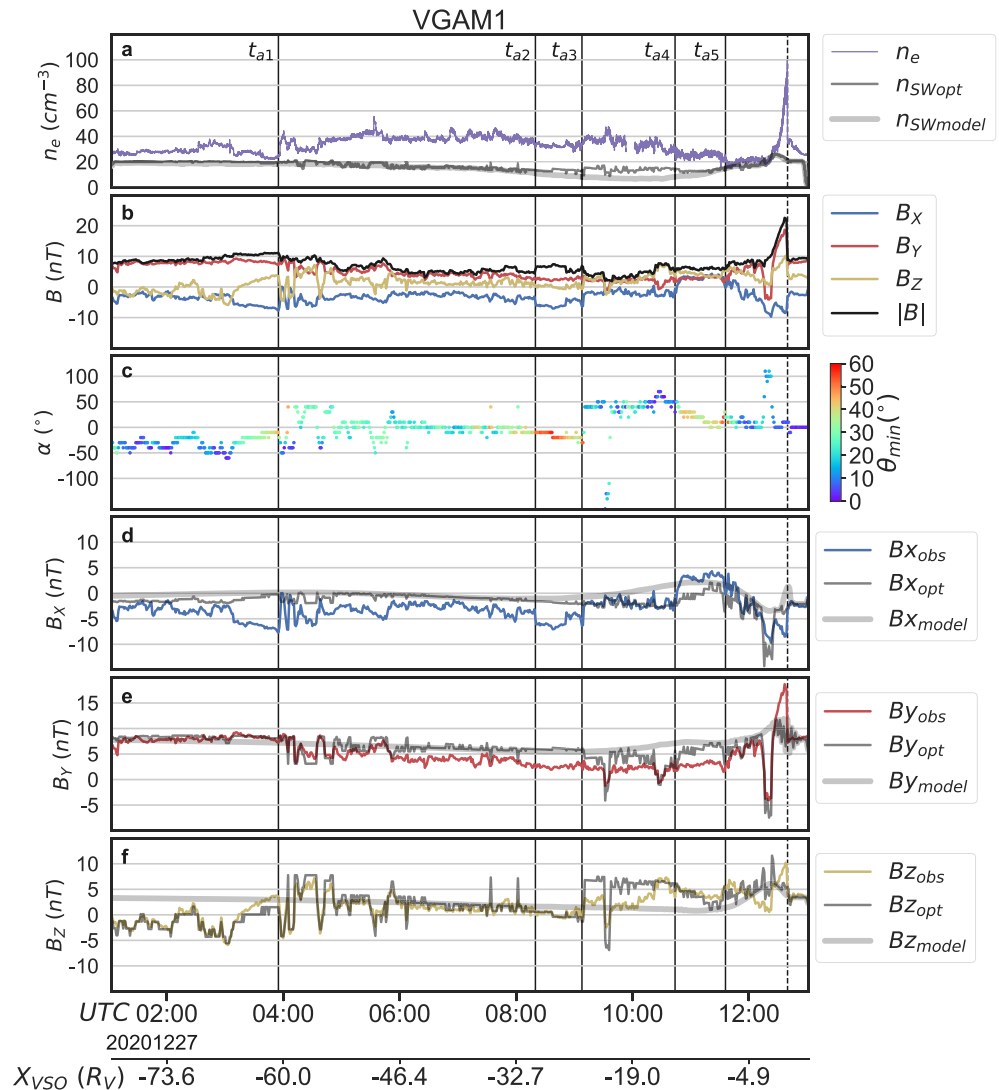
Figure 8. VGAM1 Observations-model comparison. SolO's (a) electron density (1 Hz), derived from the spacecraft potential (Khotyaintsev et al., 2021) and (b) 1 minute averages of the magnetic field components and magnitude. The default modeled and optimized proton density are also overplotted in (a). In (c) we plot model's α_{opt} with θ_{min} color-coded and in (d)–(f) the measured magnetic field components Bx_{obs}, By_{obs}, and Bz_{obs} as blue, red, and yellow solid lines, respectively with the model's default (Bx_{model}, By_{model}, Bz_{model}) and optimum (Bx_{opt}, By_{opt}, Bz_{opt}) components as fade thick and thin gray lines over-plotted are presented, respectively. UTC time of VGAM1 is plotted as the main X-axis, while the X_{VSO} coordinate is displayed as a secondary axis. The five black vertical lines labeled t_{a1}-t_{a5} indicate the points where the magnetic field behavior changes and the black dashed line represents the bow shock crossing.

in the upstream conditions. These transitions have been determined purely by eye, based on the data shown. Finally, the dashed line farthest to the right represents the bow shock crossing by the spacecraft at ~12:40 UTC.

Looking at the observed magnetic field in Figure 8b, we notice that prior to t_{a1}, the magnetic field components resemble the IMF in the sense that they appear steadier and with fewer fluctuations. What is more, the values of B_X, B_Y, and B_Z are similar to the ones upstream. The same pattern is observed in Figure 8a, where the electron density does not fluctuate as much as it does closer to the planet and values farther t_{a1} are similar to the ones we see upstream. The density jumps abruptly, where line t_{a1} is drawn, to more elevated densities which are observed until t_{a4}. The modeled plasma density appears steadier and for the greater part of VGAM1 lower than the observed electron density. The region bounded by t_{a2} and t_{a3} shows high θ_{min} (Figure 8c), up to 60°, which means that no matter how much we rotate the magnetic field, the simulation results cannot accurately reproduce the observed magnetic field in this interval. Meanwhile, the observed magnetic field in the interval between t_{a2} and t_{a3}, in
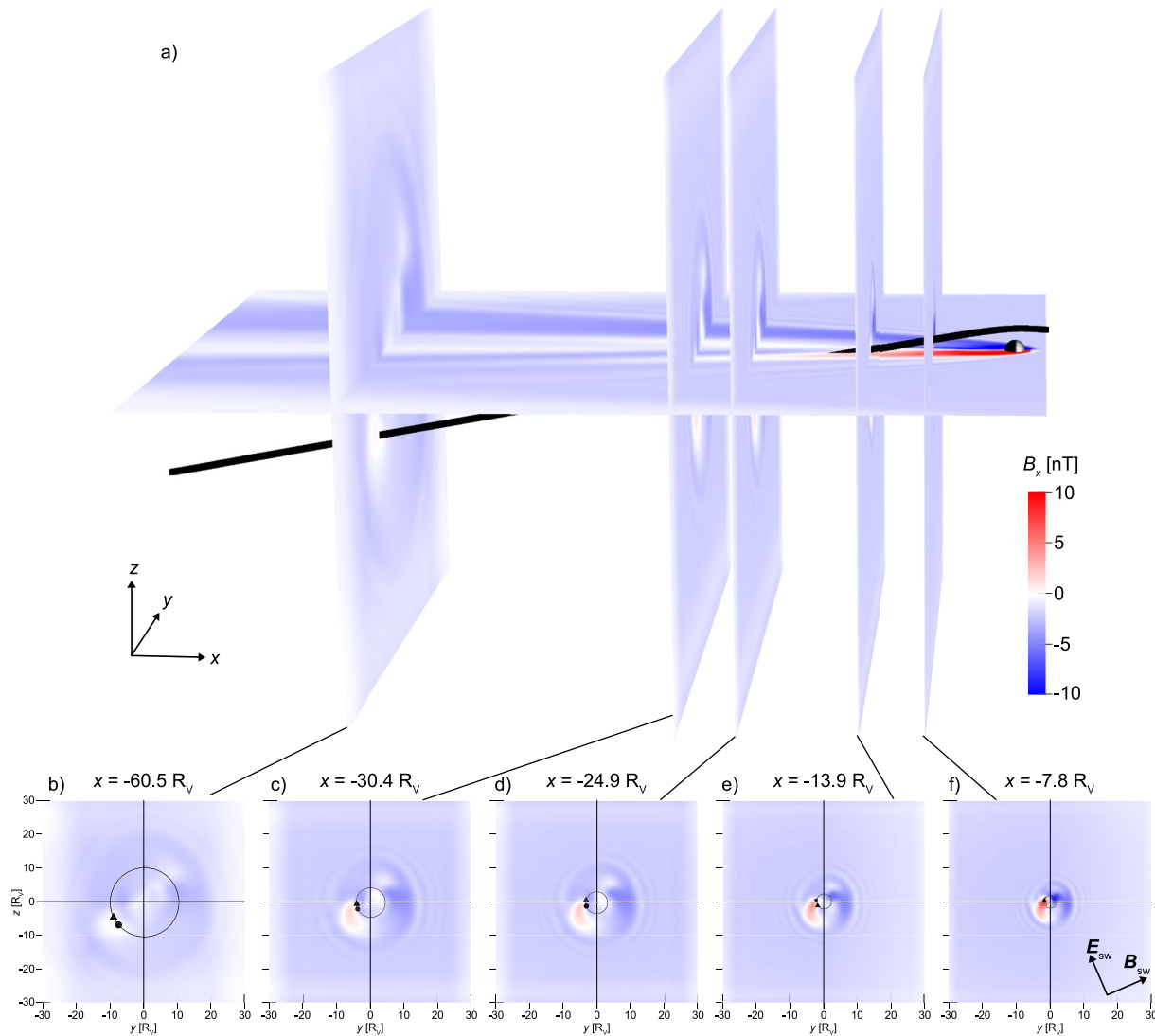
Figure 9. Simulation results of the evolution of the B_X component of the magnetic field during VGAM1. In (a), B_X is shown color-coded in the XY VSO plane, with five cuts in the YZ plane at different locations superimposed. The same five YZ plane cuts are presented in (b)–(f), with B_X color-coded. The black line in (a) depicts the VGAM1 trajectory, while the black circles and triangles in the sub-panels in (b)–(f) represent the actual position of SolO and its "optimized" location after rotation around the x-axis, respectively.

Figure 8b, becomes somewhat steadier with time and with decreased fluctuations compared to the preceding and following intervals, and at the same time the electron density shown in Figure 8a is slightly decreased with respect to the surrounding regions. Similarly, θ_{min} is also elevated at ~50° in the interval between t_{a4} and t_{a5}, and the observed magnetic field again is reasonably steady. Overall, α_{opt} in Figure 8c ranges between −50° and 50° for the greater part of the spacecraft's trajectory, while θ_{min} is mostly smaller than 40° with higher values observed only between t_{a2} and t_{a3}, and t_{a4} and t_{a5}. In Figures 8d–8f, where we overplot the observed magnetic field components with the modeled components, we notice that there is generally better agreement between Bz_{opt} and Bz_{obs} than the other two components of the magnetic field.

In Figure 9 we show the simulation results again during VGAM1, concentrating on the evolution of the B_X component of the magnetic field during the flyby. Specifically, in Figure 9a, B_X is shown color-coded on the XY VSO plane, along with five cuts through the domain in the YZ plane at different locations down the tail. These same five YZ plane cuts are then depicted in 2-D in Figures 9b–9f for clarity, again with the component B_X displayed color-coded. The black line in Figure 9a represents the VGAM1 trajectory in the VSO frame. In each sub-panel (Figures 9b–9f) we show the position of SolO as a black circle at the VSO location at which it traversed

this plane, and as a black triangle at the 'optimized' location, that is to say the position of the spacecraft in the rotated simulation domain (i.e., having the same cylindrical distance from the X-axis, but having been rotated through a clock angle α_{opt}).

Our interpretation of the plasma environments and regions encountered by SolO during VGAM1 is then as follows. Prior to t_{a1} at 03:55 UTC, SolO is in the solar wind, albeit solar wind that is likely no longer "pristine," and may even have transitioned the shock and been part of the sheath, but has likely now returned to substantial fraction of solar wind background velocity, and magnetic fluctuations have been damped or dispersed to the point that they are no longer significant (cf., Figure 2). This is moreover consistent with being in a region, irrespective of any rotation applied, where the traced magnetic field lines resulting from the situation are essentially straight and aligned with the unperturbed IMF upstream, indicating that little to no stress is being applied, and the plasma flow velocities on the field lines are everywhere similar.

From t_{a1} to t_{a2}, SolO traverses the magnetosheath. Here, the median value of the necessary rotation applied is $\alpha_{\text{opt}} = 0°$, that is, the clock angle of the magnetic field is equal to the upstream IMF, and moderately good model-data agreement can be obtained, $\theta_{\min} \sim 27°$. The B_X component is more strongly negative in the observations, possibly indicating that the "draping" of the IMF around the ionosphere and through the magnetosheath is stronger than predicted by the simulation. Between t_{a2} and t_{a3}, we see a signature that could indicate a possible excursion into the Venus plasma wake, or an effective motion of the spacecraft closer to the central axis of the interaction region. This is the same interval identified as a "tail lobe" by Hadid et al. (2021). While no substantial rotation is necessary to provide good model-data agreement upon crossing t_{a2} (indicating reasonably steady IMF orientation at this interface), there is a difference in α_{opt} of 50° across t_{a3}. Taken together, this could indicate a reduction in dynamic pressure or the IMF cone angle (the angle between the IMF vector and the X-axis) moving past Venus at t_{a2}, effectively expanding the size of the interaction region, and moving the "wake" boundary across the location of SolO, giving rise to larger B_X values observed than are predicted in the model, and a more "lobe-like" field geometry. Then, at t_{a3}, there is evidence for a rotation in the IMF, and better model-data agreement is obtained following this, suggesting SolO re-crosses the UMB and is once again in the magnetosheath.

At ~09:32 UTC there is a significant discontinuity seen in the values of α_{opt} that persists only for 4 min. This corresponds precisely to the approach to a magnetic reconnection site identified by Volwerk, Horbury, et al. (2021) labeled as "ST2". While such an explanation is found to be consistent with observations here, we do note however that continued good model-data agreement is seen in our results, with $\theta_{\min}$ essentially consistent immediately before and after, and during this discontinuity in α_{opt}, suggesting that the observed field is equally consistent also with a very brief but significant IMF rotation passing through the system. Accompanying changes in the solar wind plasma conditions can easily account for the minor variation noted in electron density during this interval.

In the interval between t_{a4} and t_{a5}, we see again generally poor model-data agreement, primarily the result of B_X being larger than predicted by the simulation for any stationary IMF clock angle case. The plasma density does appear also to drop at t_{a5}, which could correspond to the spacecraft moving into the immediate wake region of Venus. We note, as did Volwerk, Horbury, et al. (2021), that the upstream IMF was slightly less radial than nominally expected from the Parker Spiral, so a more radial field at earlier times is more likely, and consistent with such a change toward more nominal conditions prior to t_{a5}. Finally, the interval studied by Volwerk, Horbury, et al. (2021) labeled "ST4" (~12:20 UTC) and suggested to evidence "'overdraping" in the field can, again, equally well be interpreted as a transient rotation in the IMF clock angle at the same time.

5.2. VGAM2

We now follow the same process for VGAM2, again noting that we utilize the same global hybrid simulation run for data-model comparisons in this initial analysis. We believe this to be justified since the difference in the IMF magnitude and cone angle is a difference of ~18% and 10°, respectively, where the cone angle is $\theta_c = \arccos\left(\frac{B_X}{|B|}\right)$. The solar wind speed for VGAM2, measured approximately 5 hr after the shock, is ~300 km/s, which is similar to the value estimated for VGAM1 (325 km/s), and it remains at this value for several hours afterwards. Furthermore, since both flybys occurred during solar minimum we assume that small differences in the solar EUV photon rates would not significantly affect the outcome. Hence, fortuitously, the upstream conditions Venus experienced were sufficiently similar that introducing a new model run was not deemed necessary, and moreover affords direct comparison between the two flybys, by taking the same simulation run results as a starting "'guide."
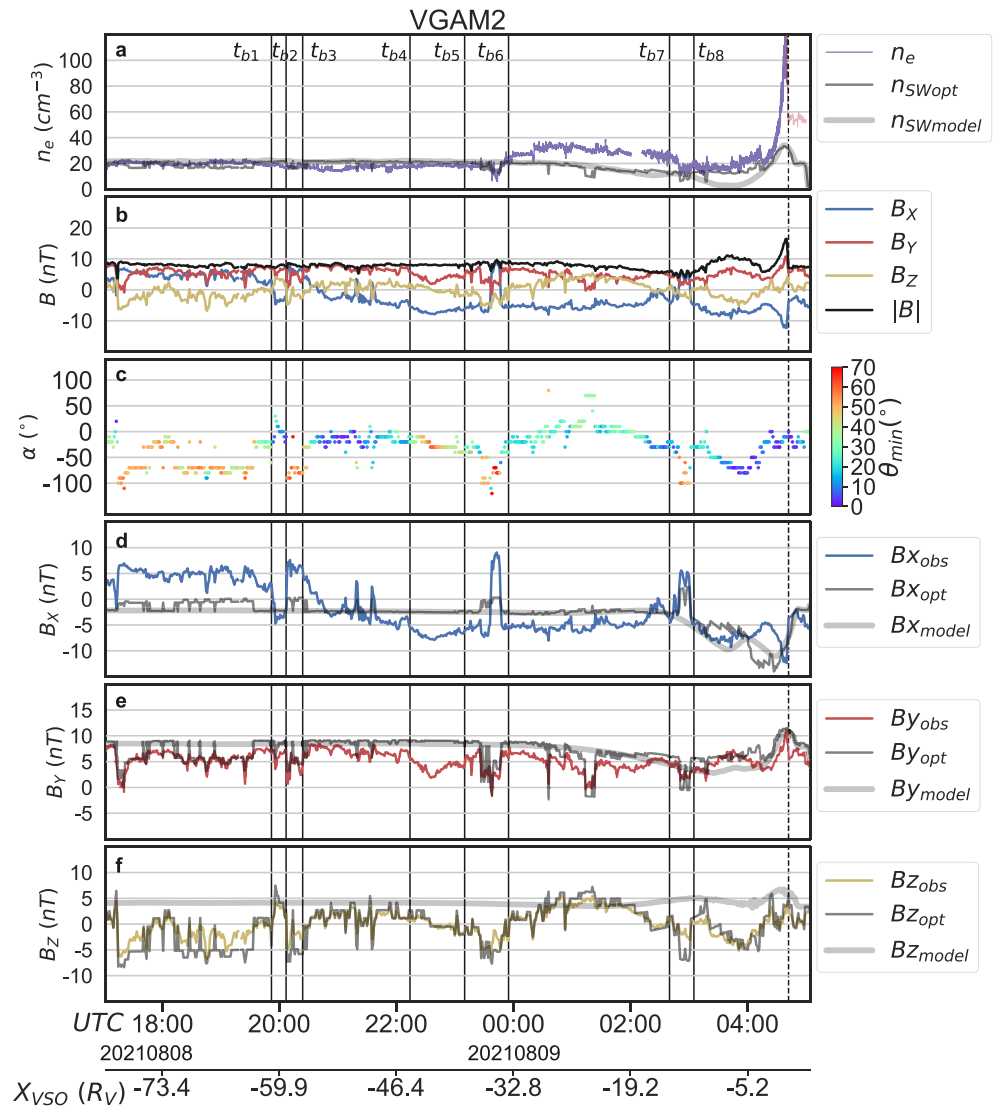
Figure 10. VGAM2 Observations-model comparison. Data are presented in a similar manner to Figure 8. The eight black vertical lines labeled t_{b1}-t_{b8} indicate the points where the magnetic field behavior changes.

In Figure 10, data from SolO and simulation results are presented in the same format as used in Figure 8. The electron density, in Figure 10a, after the spacecraft crosses the bow shock is of insufficient quality for further analysis due to instrumental problems in that interval, and hence is shown red in the plot. Utilizing the same approach applied for VGAM1, we again obtain estimates of the optimum IMF clock angle (rotation angle α_{opt}) that may be applied to the simulation to minimize the angle between the observed and modeled magnetic fields, θ_{min}, with the results shown by the colored points in Figure 10c. Throughout Figure 10 we draw eight lines labeled t_{b1}-t_{b8} to note the regions of interest, again based purely on visual inspection of these data. The outbound bow shock crossing in VGAM2 is clearly identified at ~04:41 UTC. That the upstream IMF conditions do not differ substantially between VGAM1 and VGAM2 is evident by the low values of θ_{min} obtained on VGAM2 once SolO has crossed the bow shock and entered the upstream solar wind.

During the inbound part of VGAM2, the observed magnetic field, shown in Figure 10b, does not exhibit any obvious transition from a regime resembling the solar wind as demonstrated for VGAM1 in Figure 8b. As was shown previously in Figure 3, the amplitude of magnetic field fluctuations remains lower for VGAM2 than for VGAM1, suggesting that SolO is not encountering a typical turbulent magnetosheath plasma but instead may remain relatively closer to the center of the tail and the Venus plasma wake. This is entirely possible, that is, as a result of

a relatively lower dynamic pressure and a more expanded interaction region during the earlier part of the flyby, leading to SolO being further from the bow shock despite the marginally different trajectory in this respect. Only poor agreement is found between the optimized and measured magnetic fields, θ_{min} being greater than ~50° prior to t_{b3}, with only a brief drop in values between t_{b1} and t_{b2}. The apparently bi-modal values found for α_{opt} prior to t_{b1} also indicate that no consistent agreement between the model and observations can be found for any IMF clock angle. This is largely the result of the persistent mismatch present in the B_X component, seen between the dark gray Bx_{opt} trace and the observed Bx_{obs} values themselves. Indeed, the agreement achieved in the B_X component remains generally poor throughout the whole of VGAM2. This is again consistent with the input conditions to the simulation comprising an IMF with somewhat smaller radial component than is typical at the orbit of Venus, and hence the resulting modeled B_X values being everywhere smaller in magnitude than the observations.

Following t_{b3}, the value of α_{opt} evolves smoothly throughout the remainder of the flyby, except for brief drops from values of ~−50° to ~−100° between lines t_{b5} and t_{b6}, and t_{b7} and t_{b8}. Meanwhile, the observed B_X values change from positive to negative, and remain so except within these two brief intervals. Each of these two short intervals is again coincident with an increase in the value of θ_{min} indicating relatively poor agreement between the model and the observations, and each interval is also found at the boundary of a region where the observed plasma density reaches a local maximum, between t_{b6} and t_{b7}. Complete, but transient, reversals in the X-component of the magnetic field are present in each case, consistent with SolO briefly crossing between the opposite "lobes" of the induced magnetotail. Despite the similar geometries of VGAM1 and VGAM2, only VGAM2 displays these transient apparent rotations and directly associated reductions in data-model agreement.

Interestingly, the best overall agreement between the observations and the optimized modeled components of the magnetic field is seen in B_Z in Figure 10f, as was the case in VGAM1. While the simulation results can be rotated to reproduce the observed B_Z values in both sign and magnitude throughout most of the flyby, this is only true to a lesser degree in the case of the Y-component data shown in Figure 10e, and only for a few short intervals in the case of the X-component shown in Figure 10d. The local minimum in plasma density found around t_{b8} suggests at least an approach into the immediate plasma wake of Venus by SolO, at around the same distance 5–10 R_V down-tail from the planet as was found in VGAM1. Apart from the interval between t_{b6} and t_{b7}, the modeled solar wind density in Figure 10a looks similar to the electron density from SolO.

Despite the similarities with VGAM1 in the upstream conditions, it seems clear that again a more radial IMF is dominant throughout the majority of the flyby, leading to under-predicted values of B_X throughout. While, again, no clear inbound shock crossing is detectable at large distances down-tail, SolO does appear to be in a regime dissimilar from the IMF and affected at least in part by the draping of IMF field lines around the planet throughout the interval shown in Figure 10. Overall, however, the interpretation of these data is more challenging than was found in the case of VGAM1. Looking at the magnetic field at the start and the end of the plot, we notice that they are different, particularly the B_X component. For completeness, in Figure 11, modeled B_X is presented in the same manner as in Figure 9, with sub-panels showing cuts through the simulation domain. The black line in Figure 11a represents the VGAM2 trajectory.

6. Discussion

In this study we are exploring a region where there are extremely limited observations and we take this opportunity to learn more about the tail structure. Because of the lack of measurements, we rely heavily on models to study the far tail, thus, it is important to assess the model performance in these regions using the limited data available. The two SolO Venus flybys, on 27 December 2020 (VGAM1) and 9 August 2021 (VGAM2), contributed to our view of the structure of the Venusian magnetotail, providing us with rare magnetic field and electron density data from as far as 80 R_V down the magnetotail of Venus. While future Venus flybys will be conducted with SolO, these first two are the only planned "tail" encounters; the remaining flybys will be more suited to investigate the dayside and plasma interaction regions closer to the planet itself. In this study, we analyze and compare these observations with the results of a hybrid model of the induced magnetosphere of Venus utilizing as initial conditions the upstream observations of SolO during VGAM1.

As shown in Figure 1, the two flybys have similar trajectories in the XY VSO plane, however they differ significantly in their Z coordinate. SolO upstream measurements from both flybys reveal similar IMF cone angles in the two cases, along with broadly similar solar wind densities and velocities, which allows the comparison of both flybys with the same simulation run using VGAM1's upstream conditions. The magnetic field measurements
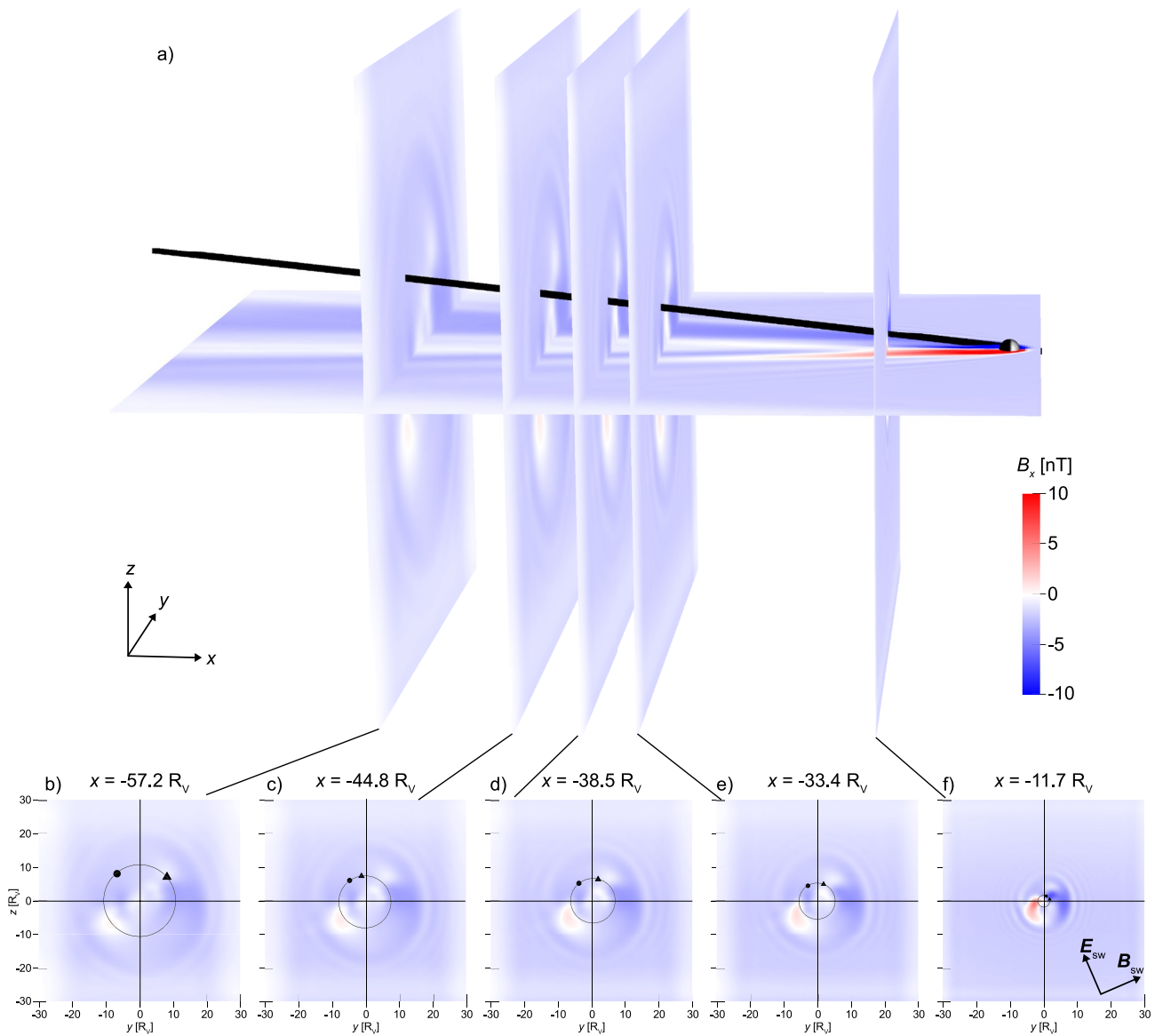
Figure 11. Simulation results of the evolution of the B_X component of the magnetic field during VGAM2, presented in a similar manner to Figure 9.

presented in Figures 2 and 3 cannot establish a consistent picture for the structure of the magnetotail, in that no immediately apparent transition from a solar wind-like field regime into a more magnetosheath-like regime is present during the inbound part of either flyby. While in VGAM1 the shape of the magnetic field changes beyond $\sim -60\,R_V$ and more fluctuations are present the closer we move to the planet, in VGAM2 there is no such an attribute seen. However, there exist in VGAM2 three regions where the B_X component changes sign abruptly implying crossings of a current sheet for a short interval before changing back.

We compare 1-min averages of the magnetic field vectors of both flybys with the vectors from the model for all the different IMF clock angles, with a 10° step, with respect to the upstream average clock angle. Collecting only the simulation vectors for which the angle between the observations and the model is minimum, we construct an optimum modeled magnetic field $\mathbf{B}_{opt}$. Based on the value of θ_{min} and the observed magnetic field behavior we also spot several regions of interest in both flybys, where the stationary change of the IMF clock angle in the simulation is not adequate to reproduce the measured magnetic field orientation.

In both VGAM1 and VGAM2, displayed in Figures 8 and 10, respectively, the model rotated to optimum clock angle seems to agree with the observations only for the B_Z component and in a lesser degree for the B_Y component.

The relatively poor agreement that can be obtained in the B_X component likely indicates that the IMF vector that was input to the initial simulation, while accurately reflecting the upstream conditions for VGAM1 post-encounter where they could be directly measured by SolO, nevertheless overestimates the "true" cone angle in the IMF for the inbound part of VGAM1 and VGAM2. A different approach where we set $B_X = 0$ in the model to investigate the degree to which the B_X component influences the structure of the induced magnetotail after comparison for example, with Venus Express data might be useful, however in this study since there is no evidence in SolO data of the X component of the magnetic field being 0 for long intervals, it did not seem necessary to attempt it.

In both VGAM1 and VGAM2, enhanced plasma densities are observed at closest approach, which, although not the focus of this paper, indicate SolO encountering the upper reaches of the planet's ionosphere, or at least approaching the density gradient at the ionopause without fully crossing it. Of more relevance here is the preceding local minimum in plasma density that is observed in case of VGAM1 in Figure 8a, approximately 8 hr prior to closest approach, at distances of ∼55 R_V down-tail, suggestive of the spacecraft moving at least partially in toward the Venus plasma wake formed toward the center of the induced magnetotail. However, that an extended but nevertheless constrained plasma structure, having a local maximum along the spacecraft trajectory, is then found tailward of this wake encounter in both VGAM1 and VGAM2 could be evidence of some detached escaping plasma structure, as has been found, for example, at Mars (Brain et al., 2010; Stergiopoulou et al., 2020), Titan (Coates et al., 2012; Edberg, Gren, et al., 2011) and previously at Venus (Brace et al., 1982; Collinson et al., 2022), albeit at closer distances. An interesting follow-up study could be a comparison with similar observations during solar maximum to see in what way the solar cycle may affect these plasma structures and if there is a correlation with the observed decrease of the escape rates of H^+ and O^+ during solar maximum (Persson et al., 2018).

The features observed in the magnetic field in the distant tail are rather different in the two flybys. In VGAM1, there appear generally steady rotations with almost constant magnitude of the magnetic field only in the IMF seen from the model-data comparison, however a distinct rotation occurs around t_{a3}, possibly following a drop in dynamic pressure (Figure 8). Structures such the ones studied by Volwerk, Horbury, et al. (2021) could be explained as transient rotations in the IMF. In VGAM2, there is a poor model-data agreement inbound prior to t_{b3}, again possibly due to the underestimated IMF radial component (Figure 10). We see three distinct rotations of the B_X component of the magnetic field (Figures 10b, 10d) and a slow change of B_X sign between t_{b3}-t_{b4}, but with reasonably constant clock angle rotation after t_{b3}, besides the two short intervals between t_{b5}-t_{b6}, and t_{b7}-t_{b8}, where poor model-data agreement occurs. Changes in B_X in the induced magnetotail could be both due to rotations in the IMF as well as changes of IMF B_X and there is no way to distinguish between those two. A time-dependent model—as opposed to the static model used in this study—could additionally demonstrate the evolution of the draped fields in the induced magnetotail of Venus particularly when features as CMEs and Corotating Interaction Regions (CIRs) encounter the planet as shown by Edberg, Nilsson, et al. (2011).

Similar features and structures in the distant magnetotail have only been observed a few times before SolO's Venus flybys, by missions such as BepiColombo and Mariner 10, which reached distances of 48 and 100 R_V down the tail, respectively. Lepping and Behannon (1978) examined Mariner's 10 measurements (5 February 1974) and reported some "disturbed" regions with rotations, increased fluctuations, and decreased magnetic field magnitudes compared to the adjacent regions, the majority of which were located no farther that 50 R_V. BepiColombo, during its first flyby, traveled in the Venusian magnetotail approximately 2 months before SolO (15 October 2020) and saw an active magnetotail with B_X rotations and flapping (Volwerk, Sánchez-Cano et al., 2021). Observations from its second flyby, albeit not from the distant induced magnetotail, were compared with a different global hybrid model in a study by Aizawa et al. (2022).

7. Conclusions

Using magnetic field and electron density observations of the first two SolO's Venus flybys and comparing them with a 3-D global hybrid simulation for the Venusian solar wind interaction, we have found that.

1. The process we follow, rotating the simulation solution to different stationary IMF clock angles, comparing with the observed magnetic field and deriving the optimum magnetic field, results in a better data-model agreement for some intervals of the flybys implying that certain features seen in the induced magnetotail can be ascribed simply to changes in the IMF clock angle.

2. In VGAM1 at distances beyond 60 R_V from the planet, solar wind starts to dominate. We see evidence that there is a transition from what appears to be more sheath-like plasma closer to the planet to the solar wind, suggesting the shock may sometimes still be present at these large distances, or at least a discontinuity remains separating these two regions.

3. In both flybys there are extended regions covering distances greater than 20 R_V where modest plasma density enhancements are observed, separated by local minima from the highest densities seen closer to the planet. These could be interpreted as detached escaping plasma "blobs" seen frequently in other induced magnetospheres.

More generally, we have shown that the unexplored distant tail is highly structured but that this structure is difficult to uniquely characterize using measurements from a single spacecraft. For similar future studies, we suggest to use hybrid or similar models to help to interpret the data, in particular by exploiting the possibility of rotating the simulation to accurately simulate time-variations in the IMF clock angle. Future studies should adopt similar approaches, where conventional trajectories and orbits can be derived that provide a more accurate model-data comparison, and may also perform higher resolution runs to provide comparisons on smaller scales. Ultimately, we also demonstrate the essential need for coordinated multi-spacecraft missions at non-terrestrial environments if we are to properly understand and interpret observations.

The understanding of small-scale features such as waves, reconnection sites, and current sheets also depend on the larger scale understanding of the system, such as identifying the correct region, and ruling out externally-imposed rotations due to changes in the IMF. Thus, this study also contributes to understanding the dataset as a whole and therefore benefits any future use of these data on small or large scales. Due to only limited single spacecraft observations from the distant induced magnetotail of Venus (and induced magnetotails in general), its structure and response to the solar wind variations has not been yet thoroughly described. Global simulations with time dependent upstream conditions and large simulation domains resolving the Venus-solar wind interaction from the dayside in the deep tail are needed. Future flybys and Venus dedicated missions, as well as multi-spacecraft missions with solar wind monitors, are essential to gaining a comprehensive understanding of the processes driving the topology of the distant Venusian induced magnetotail.

Data Availability Statement

The SolO data used in this study are available at the https://soar.esac.esa.int/soar/. Global three-dimensional hybrid simulations were performed using the RHybrid simulation platform, which is available under an open-source license by the Finnish Meteorological Institute
https://github.com/fmihpc/rhybrid/
The simulation code version used in this study is archived (under https://doi.org/10.5281/zenodo.7554587). Figures 4, 5, 9 and 11 were created using the VisIt open-source visualization tool (Childs et al., 2012). We acknowledge the computational resources provided by the Aalto Science-IT project.

References

Aizawa, S., Persson, M., Menez, T., André, N., Modolo, R., Génot, V., et al. (2022). LatHyS global hybrid simulation of the BepiColombo second Venus flyby. *Planetary and Space Science*, *218*(February), 105499. https://doi.org/10.1016/j.pss.2022.105499

Allen, R. C., Cernuda, I., Pacheco, D., Berger, L., Xu, Z. G., Freiherr Von Forstner, J. L., et al. (2021). Energetic ions in the venusian system: Insights from the first solar orbiter flyby. *Astronomy and Astrophysics*, *656*, 1–12. https://doi.org/10.1051/0004-6361/202140803

Brace, L. H., Kasprzak, W. T., Taylor, H. A., Theis, R. F., Russell, C. T., Barnes, A., et al. (1987). The ionotail of Venus: Its configuration and evidence for ion escape. *JGR Space Physics*, *92*(A1), 15–26. https://doi.org/10.1029/JA092iA01p00015

Brace, L. H., Theis, R. F., & Hoegy, W. R. (1982). Plasma clouds above the ionopause of Venus and their implications. *Planetary and Space Science*, *30*(1), 29–37. https://doi.org/10.1016/0032-0633(82)90069-1

Brain, D. A., Baker, A. H., Briggs, J., Eastwood, J. P., Halekas, J. S., & Phan, T. D. (2010). Episodic detachment of Martian crustal magnetic fields leading to bulk atmospheric plasma escape. *Geophysical Research Letters*, *37*(14), a–n. https://doi.org/10.1029/2010GL043916

Brecht, S. H., & Ledvina, S. A. (2021). An explanation of the nightside ionospheric structure of Venus. *Journal of Geophysical Research: Space Physics*, *126*(2), 1–17. https://doi.org/10.1029/2020JA027779

Childs, H., Brugger, E., Whitlock, B., Meredith, J., Ridge, O., Ahern, S., et al. (2012). Visit: An end-user tool for visualizing and analyzing very large data. In *High performance visualization—Enabling extreme-scale scientific insight* (pp. 357–410). CRC Press. https://doi.org/10.1201/b12985-29

Coates, A. J., Wellbrock, A., Lewis, G. R., Arridge, C. S., Crary, F. J., Young, D. T., et al. (2012). Cassini in Titan's tail: CAPS observations of plasma escape. *Journal of Geophysical Research*, *117*(5), 1–n. https://doi.org/10.1029/2012JA017595

Collinson, G. A., Ramstad, R., Frahm, R., Wilson, L., Xu, S., Whittlesey, P., et al. (2022). A Revised understanding of the structure of the venusian magnetotail from a high-altitude intercept with a tail ray by Parker solar probe. *Geophysical Research Letters*, *49*(1), 1–11. https://doi.org/10.1029/2021GL096485

Dimmock, A. P., Alho, M., Kallio, E., Pope, S. A., Zhang, T. L., Kilpua, E., et al. (2018). The response of the Venusian plasma environment to the passage of an ICME: Hybrid simulation results and Venus express observations. *Journal of Geophysical Research: Space Physics*, *123*(5), 3580–3601. https://doi.org/10.1029/2017JA024852

Dimmock, A. P., Khotyaintsev, Y. V., Lalti, A., Yordanova, E., Edberg, N. J. T., Steinvall, K., & Graham, D. B. (2022). Analysis of multiscale structures at the quasi-perpendicular Venus bow shock results from Solar Orbiter ' s first Venus flyby. *Astronomy & Astrophysics, A&A 660*, *A64*. https://doi.org/10.1051/0004-6361/202140954

Dubinin, E., Fraenz, M., Zhang, T. L., Woch, J., Wei, Y., Fedorov, A., et al. (2013). Plasma in the near Venus tail: Venus express observations. *Journal of Geophysical Research: Space Physics*, *118*(12), 7624–7634. https://doi.org/10.1002/2013JA019164

Edberg, N. J., Gren, K., Wahlund, J. E., Morooka, M. W., Andrews, D. J., Cowley, S. W., et al. (2011). Structured ionospheric outflow during the Cassini T55T59 Titan flybys. *Planetary and Space Science*, *59*(8), 788–797. https://doi.org/10.1016/j.pss.2011.03.007

Edberg, N. J., Nilsson, H., Futaana, Y., Stenberg, G., Lester, M., Cowley, S. W., et al. (2011). Atmospheric erosion of Venus during stormy space weather. *Journal of Geophysical Research*, *116*(9), 1–n. https://doi.org/10.1029/2011JA016749

Hadid, L. Z., Edberg, N. J., Chust, T., Píša, D., Dimmock, A. P., Morooka, M. W., et al. (2021). Solar Orbiter's first Venus flyby: Observations from the radio and plasma wave instrument. *Astronomy and Astrophysics*, *656*, 1–11. https://doi.org/10.1051/0004-6361/202140934

Horbury, T. S., O'Brien, H., Carrasco Blazquez, I., Bendyk, M., Brown, P., Hudson, R., et al. (2020). The Solar Orbiter magnetometer. *Astronomy and Astrophysics*, *642*(December), 1–11. https://doi.org/10.1051/0004-6361/201937257

Jarvinen, R., Alho, M., Kallio, E., & PulkkinenTuija, I. (2020). Oxygen ion escape from Venus is modulated by ultra-low frequency waves. *Geophysical Research Letters*, *47*(11). https://doi.org/10.1029/2020GL087462

Jarvinen, R., Brain, D. A., Modolo, R., Fedorov, A., & Holmström, M. (2018). Oxygen ion energization at Mars: Comparison of MAVEN and Mars express observations to global hybrid simulation. *Journal of Geophysical Research: Space Physics*, *123*(2), 1678–1689. https://doi.org/10.1002/2017JA024884

Jarvinen, R., Kallio, E., & Dyadechkin, S. (2013). Hemispheric asymmetries of the Venus plasma environment. *Journal of Geophysical Research: Space Physics*, *118*(7), 4551–4563. https://doi.org/10.1002/jgra.50387

Jarvinen, R., Kallio, E., & Pulkkinen, T. I. (2022). Ultra-low frequency foreshock waves and ion dynamics at Mars. *Journal of Geophysical Research: Space Physics*, *127*(5), 1–22. https://doi.org/10.1029/2021JA030078

Kallio, E., Jarvinen, R., & Janhunen, P. (2006). Venus-solar wind interaction: Asymmetries and the escape of O+ ions. *Planetary and Space Science*, *54*(13–14), 1472–1481. https://doi.org/10.1016/j.pss.2006.04.030

Khotyaintsev, Y. V., Graham, D. B., Vaivads, A., Steinvall, K., Edberg, N. J., Eriksson, A. I., et al. (2021). Density fluctuations associated with turbulence and waves: First observations by Solar Orbiter. *Astronomy and Astrophysics*, *656*, 1–13. https://doi.org/10.1051/0004-6361/202140936

Kivelson, M. G., Kennel, C. F., McPherron, R. L., Russell, C. T., Southwood, D. J., Walker, R. J., et al. (1991). Magnetic field studies of the solar wind interaction with Venus from the Galileo flyby. *Science*, *253*(5027), 1518–1522. https://doi.org/10.1126/science.253.5027.1518

Lepping, R. P., & Behannon, K. W. (1978). Mariner 10 magnetic field observations of the Venus wake. *Journal of Geophysical Research*, *83*(8), 3709. https://doi.org/10.1029/ja083ia08p03709

Luhmann, J. G. (1986). The solar wind interaction with Venus. *Space Science Reviews*, *44*(3–4), 241–306. https://doi.org/10.1007/bf00200818

Luhmann, J. G., & Cravens, T. (1991). Magnetic fields in the ionosphere of Venus. *Space Science Reviews*, *55*, 201–274. https://doi.org/10.1007/978-94-011-3300-5_4

Maksimovic, M., Bale, S. D., Chust, T., Khotyaintsev, Y., Krasnoselskikh, V., Kretzschmar, M., et al. (2020). The Solar Orbiter radio and plasma waves (RPW) instrument. *Astronomy and Astrophysics*, *642*, 1–23. https://doi.org/10.1051/0004-6361/201936214

Mangano, V., Dósa, M., Fränz, M., Milillo, A., Oliveira, J. S., Lee, Y. J., et al. (2021). BepiColombo science investigations during cruise and flybys at the Earth. *Venus and Mercury*, *217*(No. 1), 23. https://doi.org/10.1007/s11214-021-00797-9

Martinecz, C., Boesswetter, A., Fränz, M., Roussos, E., Woch, J., Krupp, N., et al. (2009). Plasma environment of Venus: Comparison of venus express ASPERA-4 measurements with 3-D hybrid simulations. *Journal of Geophysical Research E: Planets*, *114*(3), 1–15. https://doi.org/10.1029/2008JE003174

Masunaga, K., Futaana, Y., Yamauchi, M., Barabash, S., Zhang, T. L., Fedorov, A. O., et al. (2011). O+ outflow channels around Venus controlled by directions of the interplanetary magnetic field: Observations of high energy O+ ions around the terminator. *Journal of Geophysical Research*, *116*(9), 1–n. https://doi.org/10.1029/2011JA016705

McComas, D. J., Spence, H. E., Russell, C. T., & Saunders, M. A. (1986). The average magnetic field draping and consistent plasma properties of the Venus magnetotail. *Journal of Geophysical Research*, *91*(A7), 7939. https://doi.org/10.1029/ja091ia07p07939

Müller, D., St. Cyr, O. C., Zouganelis, I., Gilbert, H. R., Marsden, R., Nieves-Chinchilla, T., et al. (2020). The Solar Orbiter mission. *Astronomy & Astrophysics*, *642*, A1. https://doi.org/10.1051/0004-6361/202038467

Persson, M., Futaana, Y., Fedorov, A., Nilsson, H., Hamrin, M., & Barabash, S. (2018). H+/O+ escape rate ratio in the Venus magnetotail and its dependence on the solar cycle. *Geophysical Research Letters*, *45*(20), 10805–10811. https://doi.org/10.1029/2018GL079454

Phillips, J. L., & McComas, D. J. (1991). The magnetosheath and magnetotail of Venus. *Space Science Reviews*, *55*(1–4), 1–80. https://doi.org/10.1007/BF00177135

Rong, Z., Barabash, S., Futaana, Y., Stenberg, G., Zhang, T. L., Wan, W., et al. (2014). Morphology of magnetic field in near-Venus magnetotail: Venus express observations. *Journal of Geophysical Research: Space Physics*, *111*(11), 8838–8847. https://doi.org/10.1002/2014ja020461

Rong, Z., Barabash, S., Stenberg, G., Futaana, Y., Zhang, T. L., Wan, W., et al. (2015). The flapping motion of the Venusian magnetotail: Venus Express observations. *Journal of Geophysical Research: Space Physics*, *120*(7), 5593–5602. https://doi.org/10.1002/2015ja021317

Russell, C. T., Elphic, R. C., & Slavin, J. A. (1979a). Initial pioneer Venus magnetic field results: Dayside observations. *Science*, *203*(4401), 745–116. https://doi.org/10.1126/science.205.4401.114

Russell, C. T., Elphic, R. C., & Slavin, J. A. (1979b). Initial pioneer Venus magnetic field results: Nightside observations. *Science*, *205*(4401), 114–116. https://doi.org/10.1126/science.205.4401.114

Russell, C. T., Luhmann, J. G., Elphic, R. C., & Scarf, F. L. (1981). The distant bowshock and magnetotail of venus: Magnetic field and plasma wave observations. *Geophysical Research Letters*, *8*(7), 843–846. https://doi.org/10.1029/gl008i007p00843

Russell, C. T., Luhmann, J. G., & Strangeway, R. J. (2006). The solar wind interaction with Venus through the eyes of the pioneer Venus Orbiter. *Planetary and Space Science*, *54*(13–14), 1482–1495. https://doi.org/10.1016/j.pss.2006.04.025

Saunders, M. A., & Russell, C. T. (1986). Average dimension and magnetic structure of the distant Venus magnetotail. *Journal of Geophysical Research*, *91*(A5), 5589–5604. https://doi.org/10.1029/ja091ia05p05589

Slavin, J. A., Intriligator, D. S., & Smith, E. J. (1989). Pioneer Venus Orbiter magnetic field and plasma observations in the Venus magnetotail. *Journal of Geophysical Research*, *94*(A3), 2383. https://doi.org/10.1029/ja094ia03p02383

Stergiopoulou, K., Andrews, D. J., Edberg, N. J., Halekas, J., Kopf, A., Lester, M., et al. (2020). Mars express observations of cold plasma structures in the Martian magnetotail. *Journal of Geophysical Research: Space Physics*, *125*(10), 1–15. https://doi.org/10.1029/2020JA028056

Terada, N., Shinagawa, H., Tanaka, T., Murawski, K., & Terada, K. (2009). A three-dimensional, multispecies, comprehensive MHD model of the solar wind interaction with the planet Venus. *Journal of Geophysical Research*, *114*(9), 1–n. https://doi.org/10.1029/2008JA013937

Volwerk, M., Horbury, T. S., Woodham, L. D., Bale, S. D., Simon Wedlund, C., Schmid, D., et al. (2021). Solar Orbiter's first Venus flyby: MAG observations of structures and waves associated with the induced Venusian magnetosphere. *Astronomy and Astrophysics*, *656*, 40910. https://doi.org/10.1051/0004-6361/202140910

Volwerk, M., Sánchez-Cano, B., Heyner, D., Aizawa, S., André, N., Varsani, A., et al. (2021). Venus's induced magnetosphere during active solar wind conditions at BepiColombo's Venus 1 flyby. *Annales Geophysicae*, *39*(5), 811–831. https://doi.org/10.5194/angeo-39-811-2021

Zhang, T. L., Du, J., Ma, Y. J., Lammer, H., Baumjohann, W., Wang, C., & Russell, C. T. (2009). Disappearing induced magnetosphere at Venus: Implications for close-in exoplanets. *Geophysical Research Letters*, *36*(20), 2–6. https://doi.org/10.1029/2009GL040515